Drone-based photogrammetry combined with deep-learning to estimate hail size distributions and melting of hail on the ground

Martin Lainer[1], Killian P. Brennan[1,a], Alessandro Hering[1], Jérôme Kopp[2], Samuel Monhart[1], Daniel Wolfensberger[1], and Urs Germann[1]

[1]Federal Office of Meteorology and Climatology, MeteoSwiss, Locarno-Monti, Switzerland
[a]now at: Institute for Atmospheric and Climate Science, ETH Zurich, Zurich, 8092, Switzerland
[2]Oeschger Centre for Climate Change Research and Institute of Geography, University of Bern, Bern, Switzerland

Correspondence: Martin Lainer (martin.lainer@meteoswiss.ch)

Abstract. Hail is a major threat associated with severe thunderstorms and estimating the hail size is important for issuing warnings to the public. For the validation of existing, operational, radar-derived hail estimates, ground-based observations are necessary. Automatic hail sensors, as for example within the Swiss hail network, record the kinetic energy of hailstones to estimate the hail sizes. Due to the small size of the observational area of these sensors ($0.2\,\mathrm{m}^2$), the full hail size distribution (HSD) cannot be retrieved. To address this issue, we apply a state-of-the-art custom trained deep-learning object detection model to drone-based aerial photogrammetric data to identify hailstones and estimate the HSD. Photogrammetric data of hail on the ground was collected for one supercell thunderstorm crossing central Switzerland from southwest to northeast in the afternoon of 20 June 2021. The hail swath of this intense right-moving supercell was intercepted a few minutes after the passage at a soccer field near Entlebuch (Canton Lucerne, Switzerland) and aerial images were taken by a commercial DJI drone, equipped with a 45 megapixel full frame camera system. The resulting images have a ground sampling distance (GSD) of $1.5\,\mathrm{mm}$ per pixel, defined by the focal length of $35\,\mathrm{mm}$ of the camera and a flight altitude of $12\,\mathrm{m}$ above ground. A 2D orthomosaic model of the survey area ($750.4\,\mathrm{m}^2$) is created based on 116 captured images during the first drone mapping flight. Hail is then detected by using a region-based Convolutional Neural Network (Mask R-CNN). We first characterize the hail sizes based on the individual hail segmentation masks resulting from the model detections and investigate the performance by using manual hail annotations by experts to generate validation and test data sets. The final HSD, composed of 18207 hailstones, is compared with nearby automatic hail sensor observations, the operational weather radar based hail product MESHS (Maximum Expected Severe Hail Size) and crowdsourced hail reports. Based on the retrieved data set, a statistical assessment of sampling errors of hail sensors is carried out. Furthermore, five repetitions of the drone-based photogrammetry mission within $18.65\,\mathrm{min}$ facilitate investigations into the hail melting process on the ground.

1 Introduction

Hail is a severe hazard associated with thunderstorms and the threat and potential damage increases with increasing hail size. Therefore, the estimation of the hail size is important to issue appropriate warnings to the public and to assess the damage. Between 18 June and 31 July 2021 a period of intense hail storms occurred over Switzerland (Kopp et al., 2022). 340 million

(CHF) storm-related losses are estimated in the month of June and large hail played a significant role (la Mobilière, 2021).

25 Operational weather radar-based algorithms allow for the computation of the the maximum expected severe hail size (MESHS, Treloar, 1998) and probability of hail (PoH, Waldvogel et al., 1979) within a thunderstorm. In Switzerland, those products are derived from five C-band weather radars operating in the complex terrain of the Alps (Germann et al., 2022) and have a spatial resolution of $1\,km^2$. Ground-based observations are crucial for the verification and improvements of such radar-based hail products.

30 Besides traditional hailpads, which are cost effective but do not provide any temporal information, new automatic hail sensors (Löffler-Mang et al., 2011) and crowdsourced hail reports (Barras et al., 2019) provide valuable additional hail observations. Within the framework of the Swiss Hail Network project (Romppainen-Martius, 2022; Kopp et al., 2022) a network of 80 automatic hail sensors was installed in three hail-prone regions in Switzerland (Jura, southern Ticino and Napf) that are identified as hail hot spots based on climatological studies (Nisi et al., 2018, 2016). These sensors provide an estimate of the

35 hail size and the exact time of the impact, but no information about the shape. In addition, hail sensors cannot capture the entire hail size distribution (HSD) due to their small observational area of $0.2\,m^2$ (Kopp et al., 2023). Similarly, crowdsourced hail reports use predefined categories (no hail, $< 10\,mm$, $10\,mm$, $20\,mm$, $30\,mm$, $50\,mm$ and $> 70\,mm$) for estimating the hail size, corresponding to an unknown percentile of the actual HSD. Besides that, their quality control is challenging (Barras et al., 2019).

40 In order to overcome some of the limitations of automatic hail sensors and crowdsourced reports for estimating the HSD, a new technique, called *HailPixel*, has been introduced by Soderholm et al. (2020). They propose to use aerial imagery captured by an unmanned aerial vehicle (UAV) to survey hail on the ground over a large area. The resulting image data is analyzed using deep-learning techniques combined with computer vision feature extraction to estimate the HSD. The results from a *HailPixel* survey in San Rafael (Argentina) clearly demonstrates the advantage of this technique, as an UAV can survey an extended area

45 and capture a large sample of hailstones. They identified 15983 hailstones which allows to infer the HSD of the event.

In this study we use aerial drone images collected on 20 June 2021. That day, the ingredients for long-living and well-organized severe thunderstorms (humid air, high instability and strong wind shear) were in place across Switzerland. An air mass with steep lapse rates was advected from the southwest above a moist low-level air with mean mixing ratios around $12\,g\,kg^{-1}$. Lapse rates above the capping inversion were close to dry adiabatic. The Surface-Based Convective Available

50 Potential Energy (SBCAPE) was above $2000\,J\,kg^{-1}$ and high wind shear of about $30\,m\,s^{-1}$ in the layer 0–6 km was present at 12 UTC (Fig. 1). A supercell developed over the French Alps in the morning and moved through Switzerland within 5 hours. The track of the supercell is shown in Fig. 2(a) and was generated based on the TRT (Thunderstorm Radar Tracking) algorithm (Feldmann et al., 2023; Hering et al., 2004). From the hodograph shown in Fig. 1 a storm motion vector of $234°$ at $13\,m\,s^{-1}$ (according to Bunkers et al. (2000)) and mean storm relative winds (0–6 km) of $71°$ at $9\,m\,s^{-1}$ can be derived. This

55 environment favored the development of classical right-moving supercells (Houze et al., 1993).

The supercell produced a continuous hail swath from Lake Geneva to Zurich over a length of about $155\,km$ and the maximum hail size is estimated above $60\,mm$. Both, the maximum hail size and the hail swath are inferred from the MESHS products based on the Swiss operational radar network (Germann et al., 2022). Figure 2(b) illustrates the radar derived MESHS signature

from the supercell in the Napf region (central Switzerland) where the aerial images were collected on a soccer field (white cross) near Entlebuch (Canton Lucerne). For this location MESHS indicates a maximum expected severe hail size of $63\,\mathrm{mm}$ and on-site observations revealed maximum dimensions between $40\,\mathrm{mm}$ and $50\,\mathrm{mm}$. In addition, data from four automatic hail sensors are available for the area within $1\,\mathrm{km}$ of the survey area. Surprisingly, the closest sensor HS1 ($300\,\mathrm{m}$ SSW from the soccer field) did not record any impact during the entire hail event. Therefore, we use the data from the remaining 3 sensors in this analyses. HS2 and HS4 are located NNE of the soccer field at a distance of $770\,\mathrm{m}$ and $1470\,\mathrm{m}$, respectively, while HS3 is located SSW at a distance of $1150\,\mathrm{m}$ (Fig. 3).

Soderholm et al. (2020) provided general recommendations to optimize the quality and further analysis of aerial drone images of hail: uniform and contrasting backgrounds (cut or grazed turf grasses); high camera resolution for capturing smaller hailstones; minimize the melting of hailstones; avoid aerial surveys in areas with flowing water and conduct surveys immediately after hail fall. Following those suggestions, we achieved a ground sampling distance (GSD) of $1.5\,\mathrm{mm\,px^{-1}}$ by flying at an altitude of $12\,\mathrm{m}$ with a 45 megapixel full frame camera system. For the detailed flight and system characteristics see also Table 1. All together it permitted us to classify hailstones up to a minimum size of 3–$6\,\mathrm{mm}$, which is a significant improvement compared to the minimum size of $20\,\mathrm{mm}$ from Soderholm et al. (2020). Here, the survey was performed on a soccer field with a visually homogeneous background, and an excellent drainage of water. A main difference to the approach of Soderholm et al. (2020) is the technical setup to estimate the size of the identified hailstones. Instead of using an additional computer-vision-based method, we here only use the data from the deep-learning algorithm to estimate the hail sizes and shapes. In addition, we present an approach to address the melting of hailstones on the ground: the melting rate is estimated by capturing the shrinking of the hailstones from images of successive drone flights. This allows to approximate the expected largest hail sizes at the start of the hail fall, if the exact times of the storm passage and images are known.

In Sect. 2 the methodology is presented, starting with the data collection procedure, a description of the equipment and details about the image data acquisition, followed by the post-processing, the hail detection with deep-learning algorithms and the final retrieval of the hail size distribution. The resulting hail size distributions, performance of the model and melting rate estimation are described in Sect. 3. Further discussions to bring the findings in a broader context are presented in Sect. 4. Conclusions, ideas and suggestions for future analyses are given in Sect. 5.

2   Data and methods

In this study we use a deep-learning method to automatically detect individual hailstones in aerial images of hail. A subset of the images was annotated by a human expert and served as a training, validation and test data set. Furthermore, the test data set was annotated by two additional independent experts to objectively estimate the performance of the model. The method follows the *HailPixel* procedure described in Soderholm et al. (2020) that applies a two-stage approach, consisting of a machine learning technique to identify the center pixel of each hailstone in the image and a computer vision (CV) approach to detect the edges of the individual hailstones based on pixel lightness values. During a preliminary test in our study, the two-stage approach was compared to a one-stage method using solely a deep-learning instance segmentation model based on Mask R-

CNN to detect individual hailstones and estimate their sizes. With the two-stage approach, the edge detection did not work reliable in particular for small hailstones, because the lightness gradient between these small hailstones and the background was insufficient. Here we therefore focus on the one-stage approach.

2.1 Data collection and the experience from chasing hailstorms

A major challenge of drone-based hail photogrammetry is the collection of data. Hail producing thunderstorms are highly localized phenomena and falling hail melts quickly on the surface due to high (summer) air and soil temperature and sometimes strong rainfall following directly after the hail. Thus, to intercept a thunderstorm, the drone operators need to be on site before the arrival of the storm. Therefore, the availability of suitable nowcasting products and experienced interpretation are highly important. Aside from the meteorological challenges, the practical difficulties are even more pronounced. To obtain best possible quality of aerial images, we focused on places where we were confident to encounter fresh cut meadows. Public soccer fields turned out to be most promising target locations, which can be easily identified in interactive maps while being on the road, e.g. on https://map.geo.admin.ch/ (SwissGeoportal, 2023). In addition, major parts of the hail prone areas were scouted in advance to determine potential locations to intersect a specific storm cell and familiarize with the local traffic routes.

During days with conditions favorable for supercells, the drone operators were on standby in central Switzerland already in the morning hours to be ready to head towards potential regions of thunderstorm occurrence. A valuable source to identify such conditions and regions are the forecasts by ESTOFEX (European Storm Forecast Experiment, Groenemeijer et al. (2007)). Our experience has shown, that at least a level 2 on the ESTOFEX internal scale needs to be issued to have a realistic chance to intercept a hail producing cell. In general, the forecasts and evaluation of the synoptic situation across Europe provided on their website are highly valuable for the preparation process and determining, whether meteorological conditions are favorable on the next day.

On the day of an event, different nowcasting and observational products were used. Most importantly, the operational radar images produced by MeteoSwiss served as a baseline to identify storms and nowcast the upcoming minutes to hours. The 3-dimensional reflectivity information is crucial to not only identify the cell itself but to further estimate the strength and exact location of a potential hail core. Within the operational radar products, POH and MESHS was used. Our experience has shown that for promising results, POH needs to be 100% and MESHS should reach stable values above $20\,\mathrm{mm}$. Furthermore, satellite images and lightning information, e.g. lightning jumps (Schultz et al., 2009; Chronis et al., 2015; Nisi et al., 2020), help to focus on intensifying regions within the developing storm cells. Finally, real-time hail reports from the public can give a hint about the size of the hail that can be expected and to fine tune the final decisions for a suitable location.

Following this strategy and using the tools mentioned, two drone-based hail photogrammetry surveys could be performed during five event days in 2021. In this study, we present an analysis of the data collected on 20 June 2021 to demonstrate the methodology. The data from the second available event cannot be taken into account because of low quality of the data. In particular, both, the light conditions and the background (longer grass on the soccer field) were not optimal and thus the data can unfortunately not be used for an in depth analysis.

2.2 Drone operation and image processing

The aerial hail photogrammetry missions were performed with a DJI Matrice 300 RTK drone equipped with a Zenmuse P1 camera system, that has a full-frame sensor (45 megapixel) stabilized by a 3-axis gimbal and a focal length of $35\,\mathrm{mm}$. The synchronization of the camera, the flight controller and the gimbal is done on a temporal resolution of microseconds and thus ensures a high accuracy of the image data. The drone was not operated with enabled RTK (Real Time Kinematic) feature. This would require the installation of a RTK base station module. The advantage would be an increase in positional accuracy of the drone from the order of few decimeters to centimeters. Another potential option would be to use the NTRIP (Networked Transport of RTCM (Radio Technical Commission for Maritime Services) via Internet Protocol) protocol. This protocol facilitates the transmission of correction data over the internet. It enables real-time positioning and precise navigation by delivering accurate correction data to GPS receivers.

In a first step, the individual images captured by the drone have to be combined into an orthomosaic. An orthomosaic is defined as a composite of multiple aerial (airborne or space-borne) photos that are previously processed to remove inherent distortions caused by the geometrical properties of the lenses (airborne photos) and the earths curvature (space borne satellite images). Thus, the processed individual pictures and the resulting composed orthomosaic is distortion free and exhibits a true scale that allows to estimate the size of the objects within the photo. To generate an orthomosaic an image overlap between $70\,\%$ and $80\,\%$ is required (Guidi et al., 2020; Fawcett et al., 2019). Here we use an image overlap of $70\,\%$ for both sides (frontal and sideways).

The flight pattern was programmed using the DJI Pilot 2 application. We defined a lawnmower (boustrophedonic) flight path without cross-hatch with a flight altitude of $12\,\mathrm{m}$ above ground (minimal possible altitude) and a flight speed of $1\,\mathrm{m\,s^{-1}}$. A low horizontal flight speed is necessary to reduce the motion blur (Bemis et al., 2014; Soderholm et al., 2020), which is within one image pixel ($0.67\,\mathrm{px}$) in our case and leads in general to small overestimations ($\approx 1\,\mathrm{mm}$) of the hail dimensions. The orthomosaic (or orthophoto) is generated using the open source software OpenDroneMap (ODM, OpenDroneMap (2020)). This software can convert 2-dimensional images into: classified point clouds, 3-dimensional textured models, georeferenced orthorectified imagery or georeferenced digital elevation models. ODM makes use of OpenSfM (mapillary, 2020), which is a structure from motion (SfM) library written in Python on top of OpenCV (Bradski, 2000). The library can be used to reconstruct camera positions and 3-dimensional scenes based on multiple images (mapillary, 2023). Here we make use of the basic modules for SfM: Feature detection, feature matching, minimal solvers.

The orthophoto construction can can be divided into the following main steps:

- Identification of matching points between the images.

- Reconstruction of the camera perspective and the position of each image for quality check and subsequent computation of the 3-dimensional coordinates of the matching points.

- Derivation of a DEM (digital elevation model) by using a reduced point cloud in 3-dimensional space.

- Construction of the orthophoto by applying the DEM to the spatial projection of each image point.

The first flight started at 14:37:28 (UTC), which is about 9.5 min after the start of the hail fall. Within 3:51 min a total of 116 images were taken. Table 1 summarizes the detailed drone, camera system and flight characteristics of the hail photogrammetry mission. Although it is critical to get off the ground as soon as possible after the hailfall, environmental conditions like rain rate, wind and gust speed should be carefully watched out in order to stay within the permitted operation conditions of the drone model. The utilization of a relatively high ISO value, as outlined in Table 1, facilitates operational use even in challenging lighting conditions, maintaining low motion blur (0.67px) at a constant flight speed of the drone. Furthermore, wind and gusts can affect the drone's stability, potentially leading to additional image blurring.

Table 1. Specifications of the drone, camera system and flight characteristics.

Parameter	Value
Drone type	DJI Matrice 300 RTK
Camera type	45 MP Zenmuse P1
Image resolution	8192 px $\times$ 5460 px
Objective focal length	35 mm
ISO	25600
Exposure time	1/1000 s
Aperture	f/5.6
Flight altitude	12 m
Flight speed	1 m s^{-1}
Path type	Lawnmower (boustrophedonic)
Image overlap	70 % (frontal and sideways)
Captures	116
Survey area	750.4 m^2
Flight duration	3:51 min (full area)
GSD	1.5 mm px^{-1}
Motion blur	0.67 px

A standard output of the ODM software is a quality report. The report gives a total of 14.916.215 reconstructed dense points and a mean GPS error of 0.34 m. The orthophoto covers an area of 750.4 m^2 (see Fig. 5(a)) that shows an elevation change of 0.5 m. Multiple reference objects (see Fig. 5(b)) placed on the soccer field are used for an independent verification of the GSD. These reference objects were laminated printouts of geometric shapes in black and white, e.g. circles with a diameter of 10 mm and squares with side lengths of 75 mm. The white circles consists of 6 to 7 pixels within the orthophoto, equivalent to a diameter of 9–10.5 mm. Due to a slight overexposure in combination with the motion blur, the black circles on white background appeared approximately 1–2 pixels smaller.

2.3 Object detection and size estimation

Object detection is a computational method to automatically identify and locate different objects or semantic classes (e.g. trees, bicycles, faces) within an image or a video. A comprehensive overview of the techniques and developments in object detection over the last two decades can be found in Zou et al. (2019). In recent years, many of the latest available neural network detection engines (e.g. AlexNet, VGG, GoogleNet, ResNet, DenseNet) have been applied to object detection. For example, the Mask R-CNN (He et al., 2020), as one of the state-of-the-art models for instance object segmentation, uses a Residual Neural Network (ResNet) detection engine described in He et al. (2016) and is designed to simplify the training of substantially deep neural networks.

We used the deep-learning toolbox Detectron2 from Wu et al. (2019) as a starting point to train a model for visual hail recognition. Its flexible design allows to switch between different tasks such as object detection, instance segmentation or panoptic segmentation. It provides built-in support for popular data sets like the MS COCO (Microsoft Common Objects in Context) described in Lin et al. (2014) and contains features from Faster/Mask R-CNN: ResNet in combination with Feature Pyramid Network (FPN), Convolution 4 (C4) as single scale feature map, or a dilated convolution technique. Furthermore, Detectron2 provides ready-to-use baselines with pre-trained model weights. Here we use one set of those pre-trained model weights to train a new model for hail detection only. Thus, we only have two classes, namely hail and the image background. The model is trained using data from a single event with grass in the background (soccer field). In order to generalise the model and apply it to additional data with different backgrounds (less homogeneous grass field, crop fields, concrete surface), the model should be retrained with additional data. However, not all backgrounds are suitable, e.g. on a concrete surface (a public parking) the hail would melt much faster due to high solar irradiation that is likely prior to thunderstorms.

2.3.1 Image data preparation

The orthophoto exhibits a resolution of $24500\,\mathrm{px}$ by $22000\,\mathrm{px}$ resulting in a total of 5.39×10^8 pixels and a disk space of about $2\,\mathrm{GB}$. The ODM software provides different output formats for the orthophoto. Here we use a PNG (Portable Network Graphics) format for the subsequent analysis. As shown in Fig. 5(a) the orthophoto does not cover the entire image size, reducing the total analyzed image pixels to about $5 \times 10^8\,\mathrm{px}$. Thus, given the GSD of $1.5\,\mathrm{mm\,px^{-1}}$, the entire image covers an area of $750.4\,\mathrm{m^2}$.

The original orthophoto is divided into smaller image tiles to save computational resources during the training of the model. A reasonable compromise is a size of $500 \times 500\,\mathrm{px}$ for each tile. We use $10\,\%$ randomly selected tiles as reference data (216 tiles). This reference data is further divided into $70\,\%$ for training (150 tiles) and $15\,\%$ for the validation (33 tiles) and test data (33 tiles) respectively. These data sets are visually analyzed by an expert A, and all hailstones are annotated using the Computer Vision and Annotation Tool (CVAT, Sekachev et al. (2020)). The resulting annotation files are JSON (JavaScript Object Notation) based and store information about each image tile. This includes the path, width, height, annotation identifiers of the hailstones and the polygon coordinates defining their instance segmentation masks. Overall, the training data set contains 937, the validation data 249 and the test data set 215 hailstone annotations. To account for differences in the visually determined

Table 2. Range tested for the 3 hyper-parameters: Learning rate (LR), γ value (γ)) and batch size (BS) per image. The hyper-parameter combination of the model with the lowest validation loss after 3000 iterations are highlighted in bold font.

LR	**0.0001**	0.00025	0.0005	0.001
γ	0.1		**0.5**	
BS	128		**256**	

annotations, two more human experts (B and C) annotated the test data set independently. Thus, the test data set annotated by the experts B and C are used as a independent data source to assess the model prediction performance.

2.3.2 Hail detection and size estimation - training, validation and testing

The main concept behind deep-learning models is to split the reference data set into a training, a validation and a test data set. The training data set is used to estimate the model parameters. Within the training procedure, a validation data set is used to prevent over fitting and to assess the evolution of performance indicators during the entire training run in steps of 100 iterations. Furthermore, an independent test data set is necessary that serves as a truth against which the model results (applied to data not contained in the reference data set) and thus the model performance can be assessed. As mentioned before, we use independent test data sets where hail is visually detected by three experts (see Fig. 9).

A NVIDIA GeForce RTX 3060 Ti was used to efficiently train the Mask R-CNN model on the training data set. This GPU model has 4864 Compute Unified Device Architecture (CUDA) cores and in total $8\,\mathrm{GB}$ GDDR6 RAM available. A default configuration of Detectron2 is used to estimate a first set for the hyper-parameter tuning. We started with a base model that is pre-trained using the MS COCO data set based on ResNet and FPN. The MS COCO data set consists of about 2×10^5 annotated images with a total of 80 different object classes and it is thus an ideal starting point to train deep-learning models to recognize, label, and describe objects.

16 different training runs (*run-0* to *run-15*) were performed to assess various hyper-parameter combinations (see Table 2). Here we only vary the three hyper parameters learning rate, the gamma value and the batch size to show a concept of proof for automatic hail detection. For detailed information about the concept and additional available parameters, we refer to (Schmidhuber, 2015; Wu et al., 2023). These training runs were performed for each of the 150 image tiles in the training data set. Using two images per batch on 1 GPU, a total of 75 batches are needed which represents one epoch time, i.e. to iterate through all available image tiles. We then performed 40 epoch times resulting in a total of 3000 iterations.

During an individual training run, the validation is done every 100 iterations. Thus, for one training run with a total of 3000 iterations we obtain a temporal evolution of the scores along 30 points. Figure 6 shows the progress of total loss and the validation loss for all 16 training runs performed. The bold lines depict the run exhibiting the lowest validation loss after 40 epoch times. To chose the best model, we performed a more detailed evaluation of the model runs by means of commonly used metrics in object detection.

To assess the performance of a model, diverse metrics are available. A single score (i.e. performance metric) does provide the model performance from a certain perspective and thus different scores should be taken into account. A score compares the predicted result with the truth based on a confusion matrix (Wilks, 2011). In image classification the predicted results of an individual feature (i.e. hailstone in our case) usually does not exactly match with the truth (the same hailstone in the test data set) but the area of overlap can vary. We therefore use the Intersection over Union (IoU) ratio. The IoU ratio is defined as the ratio between the overlap and the union of the bounding box around the features in the predicted result and the truth. In our case we use the instance segmentation mask (i.e. the one segmentation mask for each individual feature) instead of the bounding box to compute the IoU ratio. The IoU ranges from 0 to 1 and a ratio of 0.5 is used to define a correct prediction and thus interpreted as a true positive (TP) result. Predicted results with a IoU less than 0.5 are thus false positive (FP) and if no results is predicted for an existing feature in the truth, it is depicted as false negative (FN). Following the standard COCO evaluation procedure, the set of IoU ratios for a TP ranges from 0.5 to 0.95 in steps of 0.05.

In machine learning, precision and recall (Eq. (1) and Eq. (2)) are commonly used (Powers, 2020). Precision depicts the number of true positive results divided by the total number of positive results. Recall refers to all true positive results divided by the number of all samples that should have been classified (i.e. as visually identified by the experts in the test data set in our case). Precision and recall can be combined in the $F1$ score in Eq. (3) (Van Rijsbergen, 1979; Goutte and Gaussier, 2005). The $F1$ score results in values from 0 to 1 where 0 indicates extremely poor performance and 1 refers to a perfect performance of the model.

$$Precision = \frac{TP}{TP + FP} \tag{1}$$

$$Recall = \frac{TP}{TP + FN} \tag{2}$$

$$F1 = 2 \cdot \frac{Precision \cdot Recall}{Precision + Recall} \tag{3}$$

Here we prioritize the precision and aim at a large portion of correct detection (TP) of hailstones and low false positive results (i.e. hail detected by the model but not present in the test data set). Thus, as a trade-off some hailstones are missed (FN) and the selected threshold does not exactly correspond to the optimal $F1$ score. A reasonable compromise between precision and recall is found at a hail confidence threshold of 0.9 for *run-3* (see Fig. 7) where $F1$ is close to 0.8 (0.85) when evaluating against the test (validation) data set. The appearance of four groups in the two plots of Fig. 7 is due to the four different learning rate values tested (Table 2).

From the 16 different training runs, *run-3* is chosen as the model to apply to the orthophoto for automatic hail detection. Thus, (*run-3*) was applied to all available image tiles (2156) and the instance segmentation masks of each detected hail object was saved in separate Python structures linked to the individual images. In total, 18209 objects were classified as hail, but two of them were discarded as they were in the very small bin size between $1\,\mathrm{mm}$ and $2\,\mathrm{mm}$. A visual evaluation of the largest objects revealed some leaves that were incorrectly classified as hail and therefore manually removed to guarantee a correct representation of the largest hail size bins in the distribution.

In the validation data set with 249 annotated hailstones, 237 are TP and 12 are FN resulting in a false negative rate ($FNR = FN/(FN + TP)$) of 4.8 %. For the test data set with 215 hailstones, 198 are TP and 17 FN which yields a FNR of 7.9 %. An additional performance metric used to describe the accuracy of a model is the mean average precision (mAP). In short, mAP depicts the average relationship between precision and recall over all IoU classes (from 0.5 to 0.95). The mAP for the validation (test) data set results in 0.53 (0.50) for the 90 % hail confidence threshold. In addition, Figure 8 shows the number distribution of the IoU for all true positive matches (hail confidence level $C_i \geq 0.9$) within the validation (blue bars) and the test (green bars) data set. The majority of the IoUs lie above 0.7, indicating a good match between the predicted hailstones and the truth. For the test data set a bi-modal distribution is found with peaks around 0.76 and 0.86.

As mentioned in the beginning, the test data set is visually classified by three independent human experts. This allows assessing the uncertainty of the test data set resulting from the visual detection of the hailstones. The hail size (in terms of major axis length) is derived from the annotated polygons in the test data set and the model output. The resulting HSD with a bin size of 3 mm are presented in Fig. 9. It shows that expert B and expert C have a peak number of hailstones within the 6–9 mm major axis hail size bins. The median value of these experts assessments is 10.5 mm. In comparison, the highest number of hailstones and the median value of expert A are found in the next higher bin class. Overall the discrepancies are largest for the smallest size bin (3–6 mm). This indicates that the orthophoto resolution is a limiting factor for reliable identification of such small hailstones by visual classification as this size class suffers from low brightness and translucent background (see also Sect. 3 and Sect. 4).

3 Results

In this section we first present the resulting hail size distribution from the first flight performed on 20 June 2021. We compare the HSD retrieved from the photogrammetric approach presented above to the HSD retrieved by four close by hail sensors (Sect. 3.1). Subsequently, we assess the sampling error of hail sensors having an observational area of $0.2\,\mathrm{m}^2$ with a sub-sample of data retrieved from the drone observation from an area of $600\,\mathrm{m}^2$ (Sect. 3.2). In Sect. 3.3, we estimate the melting rates of hail on the ground based on the evolution of the HSD from all five successive flights.

3.1 Estimation of the hail size distribution

The HSD estimated from the aerial photogrammetric data is shown in Fig. 10. The distribution contains a total number of 18207 hailstones, and the size refers to the major axis determined by the machine learning algorithm. 45 hailstones are larger than 30 mm with the largest size being 39 mm. The mode of the distribution lies in the 6–9 mm bin. Only a few hailstones are larger than 21 mm. The closest automatic hail sensor HS2 recorded 9 impacts within 3 min and a maximum hail dimension of 14 mm (Fig. 4). The duration of the event at the location of the drone survey was ~ 9.5 min. Estimated duration based on the neighboring hail sensors range from 3 min for HS2, 13 min for HS4 and 16 min for HS3. The up-scaled density of hailstones detected by the HS2 sensor is 45 hailstones per m^2, compared to 24 hailstones per m^2 on average as retrieved from the drone data. This might be related to the inherent spatial and temporal variability of hail as the automatic hail sensor is located in a

distance of about $770\,\mathrm{m}$ downstream of the area observed by the drone. In addition, the sensor detects the hail directly during the event, whereas the drone data is collected after the hail stopped to avoid the drone being damaged. Therefore, the drone data is affected by melting processes and thus tends to underestimate the hail size and in particular the number of small hailstones. Furthermore, small hailstones might not be detected within the drone data as they might partially be obscured by the grass and by low differences in the lightness values compared to the background. Lightness values come from the HSL (Hue, Saturation and Lightness) color space and range from 0 to 255. Mean lightness values (Fig. 10, orange line) for the 3–6 mm hailstones drop below 180 which is similar to the background. Size estimation based on edge detection methods that use lightness values alone, such as proposed in Soderholm et al. (2020), can thus not be applied.

The same drone-based HSD as in Fig. 10 is shown again as a function of the probability density in Fig 11(a). A gamma probability distribution function (PDF) is used to approximate the empirical HSD. The gamma PDF is most suitable to characterize the distribution of the hailstones major-axis, as shown by Ziegler et al. (1983) or Fraile et al. (1992). Overall, the gamma PDF closely follows the empirical distribution retrieved from the drone data with a median of $9\,\mathrm{mm}$ and a slight underestimation of the peak (see Fig. 11(a)). The projected hail aspect ratios indicate that the majority of hailstones are rather spherical with axis ratios greater 0.9 (Fig. 11(b)). $75\,\%$ of the hailstones have projected aspect ratios higher than 0.75.

3.2 Sampling error within automatic hail sensor data with respect to drone-based data

In this section, we estimate the probability that a randomly placed hail sensor is hit by a hailstone of a certain size. 10000 virtual hail sensors with a size of $0.2\,\mathrm{m}^2$ were distributed across an area of $600\,\mathrm{m}^2$ within the orthophoto (blue circles in Fig. 5(d)). For each virtual sensor, the HSD was derived and the individual Kernel density estimates (KDE, gray lines) are shown in Fig. 12(a). The KDE was obtained from 7817 virtual sensor areas. The remaining 2183 sensors did not have enough virtual impacts to estimate the KDE. The distribution from the entire $600\,\mathrm{m}^2$ area is shown in black, and the respective quantiles (Q25, Q50 and Q75) from all the virtual sensors in blue, red and green.

Within all virtual hail sensors only 45 hailstones with a size larger than $30\,\mathrm{mm}$ are observed and thus only $0.3\,\%$ (34 out of 10000) of the virtual sensors exhibit an impact of such large hail. $9.9\,\%$ (988) of the virtual sensors observe impacts from hail with a size larger than $20\,\mathrm{mm}$ and $65.8\,\%$ (6576) from hail with a size larger than $10\,\mathrm{mm}$. Moreover, the probability that a sensor records no impact at all is $4.7\,\%$. Figure 12(b) shows the distribution of the largest hailstone observed by each virtual sensor. The median value reaches $12\,\mathrm{mm}$ and the 95th percentile (Q95) corresponds to $24\,\mathrm{mm}$. Figure 12(c) shows the distribution of the number of hailstones observed by all virtual hail sensors and compares it with the number of observed hailstones within the four physical hail sensors. The locations of those sensors is shown on the map in Fig. 3. All physical hail sensors were within the hail path ($100\,\%$ POH region at $1 \times 1\,\mathrm{km}$ resolution).

The highest probability ($22\,\%$, see peak of histogram in Fig. 12(c)) is given by 3 impacts on a virtual sensor. The probability for zero impacts (e.g. HS1, cyan line) is $4.7\,\%$ and the probability for 9 or 10 impacts (HS2 and HS4, blue and red line, respectively) is less than $2\,\%$. 32 impacts were recorded by the third sensor (HS3), which is higher than the maximum number of impacts (12) within all virtual sensors. This indicates that the spatial variability might play an important role and/or the limitation of the drone data regarding the melting process prior to the flight might affect the estimation.

Table 3. Time slots in UTC, when the aerial pictures of the soccer middle circle ($263\,\mathrm{m}^2$) were captured for the five drone mapping flights. From the first to the last orthophoto $1119\,\mathrm{s}$ ($18\,\mathrm{min}$, $39\,\mathrm{s}$) elapsed.

Capture series	Start $[UTC]$	Stop $[UTC]$	Capture interval $[s]$	Number of hailstones
1	14:37:59	14:41:19	200	3925
2	14:43:06	14:46:25	199	3077
3	14:47:39	14:50:59	200	2511
4	14:52:07	14:55:27	200	1962
5	14:56:38	14:59:56	198	1411

3.3 Melting on the ground and implications on hail size distribution estimations

A major limitation of the drone aerial photogrammetry is its timing with respect to impact. Hail from the beginning of the event is thus already affected by melting and decrease in size until the drone observation can take place. In this section, we quantify the impact of melting by comparing the data from five successive drone flights. This allows to estimate the temporal evolution of the HSD. Figure 13 illustrates the shape evolution of two prominent hailstones during the melting process. Due to slight deviations in the derived orthophotos from varying GPS errors ($0.21\,\mathrm{m}$ to $0.5\,\mathrm{m}$) and the melting process itself, the location of the the center hail pixel changes and leads to misalignments for an individual hailstone across the successive flights. Therefore, we only use a subset of the orthophotos and select the area within the soccer middle circle, which can be unambiguously identified. The GSD between the flights stays constant at $1.5\,\mathrm{mm}\,\mathrm{px}^{-1}$, as confirmed by the reference objects.

The area of the soccer middle circle ($263\,\mathrm{m}^2$) is well defined with a radius of $9.15\,\mathrm{m}$. Within 18.65 minutes, the time between the first and the last drone flight, the number of hailstones decreased by $64\,\%$ (see Table 3). The evolution of the KDE retrieved from all individual drone flights is shown in Fig. 14. A clear shift of the peak and the upper tail to smaller major axis lengths can be observed. The shift of the plateaus on the upper tail indicate melting rates in the order of $0.5\,\mathrm{mm}\,\mathrm{min}^{-1}$.

Using this melting rate estimate together with the time difference between the start of the hailstorm and the first drone flight, we infer that the initial size of the largest captured hailstone ($39\,\mathrm{mm}$) was $44\,\mathrm{mm}$. Most crowdsourced reports in the vicinity of the soccer field indicated sizes from $30\,\mathrm{mm}$ to $50\,\mathrm{mm}$ and the MESHS estimate was $63\,\mathrm{mm}$ (see Fig. 2(b)). On site measurements by the storm chasers during the hail event revealed maximum hail dimensions between 40 and $50\,\mathrm{mm}$ as well.

4 Discussion

A major challenge for drone-based photogrammetry of hail is related to the appearance of the hail within an orthophoto. The hailstones need to show distinct differences from the background. This is not always the case as hail is formed by a combination of dry and wet growth processes, which can lead to varying densities and appearances in the ice. Dry growth produces high densities of microscopic air bubbles that scatter light, while wet growth causes liquid to soak into gaps and accretes on top of existing outer ice to form clearer ice. Hailstones can grow in both regimes, leading to alternating layers of cloudy and clear

ice (Allen et al., 2020; Kumjian and Lombardo, 2020; Brook et al., 2021). The effectiveness of various methods used to detect hailstones is influenced, in part, by the transparency of the ice.

First, a simple computer vision approach (without neural networks) was tested to extract the segmentation hail masks. The approach was based on lightness thresholds, morphological transformations and watershed algorithms (Najman and Schmitt, 1994) for image segmentation within OpenCV (Bradski, 2000). The success and reliability of this approach highly depended on the visual appearance of the hailstones. For larger hail exhibiting distinct lightness difference compared to the background, this approach is promising. But for small hailstones exhibiting lower lightness values (Fig. 10), the CV-based edge detection (see Sect. 1 and 5) failed. For hail events with different characteristics, e.g. with a high number of small hailstones that aggregate in clusters on the ground, watershed algorithms could retrieve more reliable information.

Second, a deep-learning model (Mask R-CNN) was tested. We used one single hail class to train the model. Additional hail size classes might improve the hail predictions and mask shapes. In particular, a distinction between damaging and non-damaging hail with a threshold of $20\,\mathrm{mm}$ could be worth to test. Furthermore, additional testing of the hyper-parameters might increase the performance, but this was out of the scope of this study.

Another technical challenge arises from splitting the orthophoto into smaller image tiles which can result in truncated hailstones. This can be overcome by producing overlapping tiles by the maximum length of the largest observed hailstone, as implemented by Soderholm et al. (2020). However in our case large hail was sparse and, as the image tiles cover large areas (500×500 pixels), it is safe to assume that the number of truncated hailstones is very low. Other sources of errors such as false positive detections or missed hailstones likely play a more important role.

Hailstones usually have an oblate spheroid shape with mean axis ratios close to 0.8, though they can sometimes have large protuberances (Knight, 1986) and the probability for nonspherical shapes rises with increasing maximum dimension (Shedd et al., 2021). As a consequence the hail aspect ratio decreases for larger sizes as shown in the various studied data sets (Knight, 1986; Soderholm et al., 2020; Shedd et al., 2021). Figure 6 in Shedd et al. (2021) compares their recent results on the evolution of aspect ratios with maximum hail sizes from manually measured hailstones to the results of Knight (1986). The slopes of the decreasing aspect ratios are comparable, but the absolute values tend to be lower in the hail data set of Shedd et al. (2021), reflecting possible effects by melting before the measurements were taken. Likewise with hailpads, the shape factor in the image plane can be determined with the aerial drone-based hail photogrammetry, but the estimated aspect ratios (Fig. 11(b)) may differ from in-situ measurements as published in Knight (1986); Shedd et al. (2021). The hail images show only the projected maximum and minimum axes, which may differ to the true stone axis ratios.

Another limitation of the drone-based photogrammetry is that melting already affects the hail before the data can be collected. The effect of melting hail in the air was studied by Kumjian and Ryzhkov (2008) using polarimetric radar measurements and numerical model investigations were performed by Fraile et al. (2003). Other studies by Rasmussen and Pruppacher (1982) and Rasmussen and Heymsfield (1987) have explored the melting of spherical ice particles falling at terminal velocity. They found that the melting rate depends on the initial size of the spheres size and the surroundings, including temperature, humidity, turbulence, and how meltwater is shed. The hailstones in our case are already on the ground, so they experience different

environmental conditions compared to when they are falling through the atmosphere. We have not measured these specific conditions for each hailstone, so we cannot make any conclusions about how the melting rate relates to their initial size.

To our knowledge there are no studies that analyze the melting of a large sample size of hail on the ground. We here provide a first estimate about the melting process of hail on the ground. More in-depth investigations would be needed to retrieve more accurate results, maybe also in relation to initial hail sizes and environmental conditions like ground temperature and occurrence of rain before, during and after the hail event.

In the time series plot of Fig. 15, the evolution of temperature and relative humidity for two SwissMetNet (SMN) weather stations (Schüpfheim and Langnau i.E.) is shown between 14:00 and 15:30 UTC, alongside the time information from the drone flights and the beginning of hailfall at the soccer field in Entlebuch. The stations are located in a distance of $5.7\,\mathrm{km}$ (Schüpfheim) and $20\,\mathrm{km}$ (Langnau i.E.) to the soccer field. Unfortunately, no in-situ measurements are available for this event. Closest precipitation measurements from an automatic rain gauge (Station: Entlebuch) are available at a distance of $670\,\mathrm{m}$ to the east. $9.1\,\mathrm{mm}$ were recorded between 14:30 and 14:40 UTC and $0.2\,\mathrm{mm}$ in the subsequent 10 minutes. Thus, the hail on the ground was exposed to strong rain, which might affect the melting rate. At the same time temperatures close to the ground decreased by about $4.5\,^{\circ}\mathrm{C}$ between 14:00 UTC and 14:30 UTC, after the supercell passed the SMN station Langnau i.E. which is assumed to be in a similar range for the soccer field. To better assess the melting process, future drone-based hail surveys should include a mobile weather station or some ground temperature sensors at the observation site.

5 Conclusions and outlook

Reliable ground truth data from hail observations are rare and of high value to the hail research community. This paper assesses an application of aerial drone-based photogrammetry combined with a state-of-the-art deep-learning object detection model to retrieve the hail size distribution over a large area. The HSD retrieved from a large survey area allows to capture a representative distribution and can thus serve as a complementary source to existing ground-based observation networks such as automatic hail sensors and crowdsourced reports.

During a period in June 2021, exceptionally strong convective storms occurred in Switzerland. On 20 June 2021 drone-based photogrammetric data of a hail event related to a right-moving supercell was collected near Entlebuch (Canton Lucerne, Switzerland). Five successive drone-based photogrammetry flights were performed above a soccer field between 14:38 and 15:00 UTC. A deep-learning instance segmentation model (Mask R-CNN) under the Detectron2 framework was trained to automatically retrieve the hail size distribution.

The key results and conclusions are listed below:

- A robust retrieval of a HSD based on 18207 hailstones on an area of $750.4\,\mathrm{m}^2$ from a single hail event with a duration of about 9.5 minutes is presented. The median hailstone size was $9\,\mathrm{mm}$ and the majority of hailstones were rather spherical with axis ratios greater 0.9.

- The largest hailstone was $39\,\mathrm{mm}$ and is substantially larger than estimates retrieved from close-by automatic hail sensors.

- A combination of hail data from different sources (drone, automatic hail sensors and crowdsourced reports) to observe hail on the ground improves the reconstruction of the complete HSD and allows to assess the limitations of each method. Furthermore, such ground truth data can help to verify and further develop radar-based hail estimations.

- The analysis of virtual hail sensors placed in the photogrammetric data highlights the challenge to observe a representative sample of the HSD using a device with an area ($0.2\,\mathrm{m}^2$) much smaller than a typical hail swath.

- The evolution of the HSD caused by melting could be monitored for a period of $18.65\,\mathrm{min}$ by analysing data from multiple drone flights. A melting rate in the order of $0.5\,\mathrm{mm\,min^{-1}}$ could be estimated.

Radar-based hail algorithms estimating the size of hail, such as MESHS, need ground-based measurements for verification and potential improvements. Drone-based photogrammetry can cover areas closer to the radar spatial resolution, which makes this approach particularly valuable for the verification of radar products.

The comparison of drone-based photogrammetry with automatic hail sensors allowed to highlight the advantages and limitations of both approaches in measuring hail (see a summary in Table 4). We here want to highlight that the clustering problem refers to many hailstones that aggregate on the ground next to each other. This predominantly occurs during hail events with dominating small hail and intense precipitation. The resulting hail clusters pose a problem to the algorithm to differentiate between individual hailstones. An equivalent problem within the automatic hail sensor data is related to the dead time after each hail impact. The dead time is necessary to avoid any interference with subsequent impacts and to perform the retrieval of the data (Kopp et al., 2023). Furthermore, by combining data from both approaches strongly improves the reconstruction of the complete HSD and could further extend our understanding of hailstorms.

Future drone-based aerial photogrammetry for hail could be improved by having an artificial light source. Poor light conditions are a main challenge caused by the thunderstorm itself or if the hail occurs during twilight or night. The light conditions determine the exposure time which limits the maximum flight velocity to keep the motion blur at the same level. A flash or additional light source allows for an increased flight velocity, and thus a larger area can be covered. In addition, the image quality can be improved by reducing the sensor gain (ISO) and the aperture size. Other ideas to test and potentially improve the techniques in the future are:

- Integration of thermal imagery to help exclude or include potential hailstones alongside the RGB image processing.

- Usage of SfM (Structure from Motion) results and application of Mask R-CNN directly to mesh or point clouds instead to the RGB orthophotos.

- Fine tuning of hardware settings and flight characteristics for optimal image quality in conjunction with an acceptable motion blur.

To further assess the hail size distribution of different storms, more observational data is crucial. However, the collection of drone-based aerial photography of hail is a time-consuming and challenging task. Therefore, it could be beneficial to set up a public database of performed drone-based hail surveys to enhance collaborations between different research groups on

Table 4. Advantages (bold font) and disadvantages (normal font) of the two hail observation methods: Drone-based photogrammetry and automatic hail sensor.

	Drone-based photogrammetry	**Automatic hail sensor**
Sampling error	**low**	high
Melting problems	yes	**no**
Exact time information	no	**yes**
Probability to capture largest hailstones	**high**	low
Daylight dependence	yes	**no**
Operational application	challenging	**reasonable**
Clustering problems	high	**existing, but low**
Size estimation	**direct**	indirect

450 adaptation and testing of existing algorithms for various hail events. Moreover, with the increasing use of personal drones equipped with cameras, there could be a public community that brings the basic requirements for such observations. It might thus be useful to provide the information about how to collect adequate image data and collect such data in a crowdsourced approach similar to the existing crowdsourced reporting systems at weather services (e.g. Federal Office for Meteorology and Climatology MeteoSwiss or German Weather Service DWD). Another point to address are tests with artificial hail objects of

455 defined size classes on different backgrounds. In this way several setups could be trained, tested and optimized: Save drone operation in various conditions, flight missions and camera settings and precise comparison of the retrieved HSD to the known ground truth.

Data availability. The data collections from the hail event on 20 June 2021 analyzed in this work are publicly available from https://doi.org/10.5281/zenodo.10609730 (Lainer, 2024).

460 *Author contributions.* ML performed the following roles: conceptualization, methodology, software, validation, hail annotation, formal analysis, visualization, and writing the original draft. KB performed the following roles: conceptualization, methodology, storm chasing, drone operations, review and editing. AH performed the following roles: PI hail sensors, review and editing. JK performed the following roles: automatic hail sensor data preparation, review and editing. SM performed the following roles: conceptualization, methodology, storm chasing, hail annotation, review and editing, and project administration. DW performed the following roles: conceptualization, methodology, hail

465 annotation, review and editing. UG performed the following roles: initiation of hail research projects, acquisition of funding, procurement of equipment, review and editing.

Competing interests. All author declare to have no competing interests.

Acknowledgements. Hail is a severe threat to the society and on-going research is important to be able to establish risk mitigation measures. In this context, we thank the Swiss insurance company La Mobilière for funding the installation and operation of the automatic hail sensor network and for making the hail sensor data available for research investigations. We want to acknowledge the fruitful scientific exchange with Joshua Soderholm (Australian Bureau of Meteorology) about drone-based hail photogrammetry.

470

References

Allen, J. T., Giammanco, I. M., Kumjian, M. R., Jurgen Punge, H., Zhang, Q., Groenemeijer, P., Kunz, M., and Ortega, K.: Understanding Hail in the Earth System, Reviews of Geophysics, 58, e2019RG000 665, https://doi.org/10.1029/2019RG000665, 2020.

475 Barras, H., Hering, A., Martynov, A., Noti, P.-A., Germann, U., and Martius, O.: Experiences with >50,000 Crowdsourced Hail Reports in Switzerland, Bulletin of the American Meteorological Society, 100, 1429–1440, https://doi.org/10.1175/BAMS-D-18-0090.1, 2019.

Bemis, S. P., Micklethwaite, S., Turner, D., James, M. R., Akciz, S., Thiele, S. T., and Bangash, H. A.: Ground-based and UAV-Based photogrammetry: A multi-scale, high-resolution mapping tool for structural geology and paleoseismology, Journal of Structural Geology, 69, 163–178, https://doi.org/10.1016/j.jsg.2014.10.007, 2014.

480 Bradski, G.: The OpenCV Library, Dr. Dobb's Journal of Software Tools, 2000.

Brook, J. P., Protat, A., Soderholm, J., Carlin, J. T., McGowan, H., and Warren, R. A.: HailTrack—Improving Radar-Based Hailfall Estimates by Modeling Hail Trajectories, Journal of Applied Meteorology and Climatology, 60, 237–254, https://doi.org/10.1175/JAMC-D-20-0087.1, 2021.

Bunkers, M. J., Klimowski, B. A., Zeitler, J. W., Thompson, R. L., and Weisman, M. L.: Predicting Supercell Motion Using a New Hodograph

485 Technique, Weather and Forecasting, 15, 61–79, https://doi.org/https://doi.org/10.1175/1520-0434(2000)015<0061:PSMUAN>2.0.CO;2, 2000.

Chronis, T., Carey, L. D., Schultz, C. J., Schultz, E. V., Calhoun, K. M., and Goodman, S. J.: Exploring Lightning Jump Characteristics, Weather and Forecasting, 30, 23–37, https://doi.org/10.1175/WAF-D-14-00064.1, 2015.

Fawcett, D., Azlan, B., Hill, T. C., Kho, L. K., Bennie, J., and Anderson, K.: Unmanned aerial vehicle (UAV) derived structure-from-motion

490 photogrammetry point clouds for oil palm (Elaeis guineensis) canopy segmentation and height estimation, International Journal of Remote Sensing, 40, 7538–7560, https://doi.org/10.1080/01431161.2019.1591651, 2019.

Feldmann, M., Hering, A., Gabella, M., and Berne, A.: Hailstorms and rainstorms versus supercells—a regional analysis of convective storm types in the Alpine region, npj Climate and Atmospheric Science, 6, 19, https://doi.org/10.1038/s41612-023-00352-z, 2023.

Fraile, R., Castro, A., and Sánchez, J.: Analysis of hailstone size distributions from a hailpad network, Atmospheric Research, 28, 311–326,

495 https://doi.org/10.1016/0169-8095(92)90015-3, 1992.

Fraile, R., Castro, A., López, L., Sánchez, J. L., and Palencia, C.: The influence of melting on hailstone size distribution, Atmospheric Research, 67–68, 203–213, https://doi.org/10.1016/S0169-8095(03)00052-8, 2003.

Germann, U., Boscacci, M., Clementi, L., Gabella, M., Hering, A., Sartori, M., Sideris, I. V., and Calpini, B.: Weather Radar in Complex Orography, Remote Sensing, 14, https://doi.org/10.3390/rs14030503, 2022.

500 Goutte, C. and Gaussier, E.: A Probabilistic Interpretation of Precision, Recall and F-Score, with Implication for Evaluation, in: Advances in Information Retrieval, edited by Losada, D. E. and Fernández-Luna, J. M., pp. 345–359, Springer Berlin Heidelberg, Berlin, Heidelberg, 2005.

Groenemeijer, P., Tuschy, H., van der Velde, O., Dahl, J., and Gatzen, C.: European Storm Forecast Experiment, 2007.

Guidi, G., Shafqat Malik, U., and Micoli, L. L.: Optimal Lateral Displacement in Automatic Close-Range Photogrammetry, Sensors, 20,

505 https://doi.org/10.3390/s20216280, 2020.

He, K., Zhang, X., Ren, S., and Sun, J.: Deep Residual Learning for Image Recognition, in: 2016 IEEE Conference on Computer Vision and Pattern Recognition (CVPR), pp. 770–778, https://doi.org/10.1109/CVPR.2016.90, 2016.

He, K., Gkioxari, G., Dollár, P., and Girshick, R.: Mask R-CNN, IEEE Transactions on Pattern Analysis and Machine Intelligence, 42, 386–397, https://doi.org/10.1109/TPAMI.2018.2844175, 2020.

510 Hering, A., Morel, C., Galli, G., Sénési, S., Ambrosetti, P., and Boscacci, M.: Nowcasting thunderstorms in the Alpine region using a radar based adaptive thresholding scheme, in: Proceedings of the 3rd European Conference on Radar in Meteorology and Hydrology, 6, 2004.

Houze, R. A., Schmid, W., Fovell, R. G., and Schiesser, H.-H.: Hailstorms in Switzerland: Left Movers, Right Movers, and False Hooks, Monthly Weather Review, 121, 3345–3370, https://doi.org/10.1175/1520-0493(1993)121<3345:HISLMR>2.0.CO;2, 1993.

Knight, N. C.: Hailstone Shape Factor and Its Relation to Radar Interpretation of Hail, Journal of Climate and Applied Meteorology, 25, 515 1956–1958, http://www.jstor.org/stable/26183454, 1986.

Kopp, J., Schröer, K., Schwierz, C., Hering, A., Germann, U., and Martius, O.: The summer 2021 Switzerland hailstorms: weather situation, major impacts and unique observational data, Weather, n/a, n/a, https://doi.org/10.1002/wea.4306, 2022.

Kopp, J., Manzato, A., Hering, A., Germann, U., and Martius, O.: How observations from automatic hail sensors in Switzerland shed light on local hailfall duration and compare with hailpads measurements, Atmospheric Measurement Techniques Discussions, 2023, 1–32, 520 https://doi.org/10.5194/amt-2023-68, 2023.

Kumjian, M. R. and Lombardo, K.: A Hail Growth Trajectory Model for Exploring the Environmental Controls on Hail Size: Model Physics and Idealized Tests, Journal of the Atmospheric Sciences, 77, 2765–2791, https://doi.org/10.1175/JAS-D-20-0016.1, 2020.

Kumjian, M. R. and Ryzhkov, A. V.: Polarimetric Signatures in Supercell Thunderstorms, Journal of Applied Meteorology and Climatology, 47, 1940–1961, https://doi.org/10.1175/2007JAMC1874.1, 2008.

525 la Mobilière: 2021 Annual Report in brief, Tech. rep., Mobilière Holding Ltd., Berne, 2021.

Lainer, M.: Hail Event on 2021-06-20 in Entlebuch (LU), Switzerland: Drone Photogrammetry Imagery, Hail Sensor Recordings, Mask R-CNN Model and Analysis Data of Hailstones, https://doi.org/10.5281/zenodo.10609730, 2024.

Lin, T.-Y., Maire, M., Belongie, S., Bourdev, L., Girshick, R., Hays, J., Perona, P., Ramanan, D., Zitnick, C. L., and Dollár, P.: Microsoft COCO: Common Objects in Context, https://doi.org/10.48550/ARXIV.1405.0312, 2014.

530 Löffler-Mang, M., Schön, D., and Landry, M.: Characteristics of a new automatic hail recorder, Atmospheric Research, 100, 439–446, https://doi.org/10.1016/j.atmosres.2010.10.026, 5th European Conference on Severe Storms, 2011.

mapillary: OpenSfM, https://github.com/mapillary/OpenSfM, 2020.

mapillary: OpenSFM, https://github.com/mapillary/OpenSfM/blob/main/README.md, 2023.

May, R. M., Arms, S. C., Marsh, P., Bruning, E., Leeman, J. R., Goebbert, K., Thielen, J. E., Bruick, Z. S., and Camron, M. D.: MetPy: A 535 Python Package for Meteorological Data, https://doi.org/10.5065/D6WW7G29, 2023.

Najman, L. and Schmitt, M.: Watershed of a continuous function, Signal Processing, 38, 99–112, https://doi.org/10.1016/0165-1684(94)90059-0, mathematical Morphology and its Applications to Signal Processing, 1994.

Nisi, L., Martius, O., Hering, A., Kunz, M., and Germann, U.: Spatial and temporal distribution of hailstorms in the Alpine region: a long-term, high resolution, radar-based analysis, Quarterly Journal of the Royal Meteorological Society, 142, 1590–1604, 540 https://doi.org/10.1002/qj.2771, 2016.

Nisi, L., Hering, A., Germann, U., and Martius, O.: A 15-year hail streak climatology for the Alpine region, Quarterly Journal of the Royal Meteorological Society, 144, 1429–1449, https://doi.org/10.1002/qj.3286, 2018.

Nisi, L., Hering, A., Germann, U., Schroeer, K., Barras, H., Kunz, M., and Martius, O.: Hailstorms in the Alpine region: Diurnal cycle, 4D-characteristics, and the nowcasting potential of lightning properties, Quarterly Journal of the Royal Meteorological Society, 146, 545 4170–4194, https://doi.org/10.1002/qj.3897, 2020.

OpenDroneMap: ODM - A command line toolkit to generate maps, point clouds, 3D models and DEMs from drone, balloon or kite images, https://github.com/OpenDroneMap/ODM, 2020.

Powers, D. M. W.: Evaluation: from precision, recall and F-measure to ROC, informedness, markedness and correlation, CoRR, abs/2010.16061, https://arxiv.org/abs/2010.16061, 2020.

Rasmussen, R. and Pruppacher, H. R.: A Wind Tunnel and Theoretical Study of the Melting Behavior of Atmospheric Ice Particles. I: A Wind Tunnel Study of Frozen Drops of Radius < 500 μm, Journal of Atmospheric Sciences, 39, 152–158, https://doi.org/https://doi.org/10.1175/1520-0469(1982)039<0152:AWTATS>2.0.CO;2, 1982.

Rasmussen, R. M. and Heymsfield, A. J.: Melting and Shedding of Graupel and Hail. Part I: Model Physics, Journal of Atmospheric Sciences, 44, 2754–2763, https://doi.org/10.1175/1520-0469(1987)044<2754:MASOGA>2.0.CO;2, 1987.

Romppainen-Martius, O.: The Swiss Hail Network, https://www.mobiliarlab.unibe.ch/research/applied_research_on_hail_and_wind_gusts/the_swiss_hail_network/index_eng.html, 2022.

Schmidhuber, J.: Deep learning in neural networks: An overview, Neural Networks, 61, 85–117, https://doi.org/https://doi.org/10.1016/j.neunet.2014.09.003, 2015.

Schultz, C. J., Petersen, W. A., and Carey, L. D.: Preliminary Development and Evaluation of Lightning Jump Algorithms for the Real-Time Detection of Severe Weather, Journal of Applied Meteorology and Climatology, 48, 2543–2563, https://doi.org/10.1175/2009JAMC2237.1, 2009.

Sekachev, B., Manovich, N., Zhiltsov, M., Zhavoronkov, A., Kalinin, D., Hoff, B., TOsmanov, Kruchinin, D., Zankevich, A., DmitriySidnev, Markelov, M., Johannes222, Chenuet, M., a andre, telenachos, Melnikov, A., Kim, J., Ilouz, L., Glazov, N., Priya4607, Tehrani, R., Jeong, S., Skubriev, V., Yonekura, S., vugia truong, zliang7, lizhming, and Truong, T.: opencv/cvat: v1.1.0, https://doi.org/10.5281/zenodo.4009388, 2020.

Shedd, L., Kumjian, M. R., Giammanco, I., Brown-Giammanco, T., and Maiden, B. R.: Hailstone Shapes, Journal of the Atmospheric Sciences, 78, 639–652, https://doi.org/https://doi.org/10.1175/JAS-D-20-0250.1, 2021.

Soderholm, J. S., Kumjian, M. R., McCarthy, N., Maldonado, P., and Wang, M.: Quantifying hail size distributions from the sky – application of drone aerial photogrammetry, Atmospheric Measurement Techniques, 13, 747–754, https://doi.org/10.5194/amt-13-747-2020, 2020.

SwissGeoportal: Swiss Geoportal, https://map.geo.admin.ch/, 2023.

Treloar, A.: Vertically integrated radar reflectivity as an indicator of hail size in the greater Sydney region of Australia, in: Preprints, 19th Conf. on Severe Local Storms, Minneapolis, MN, Amer. Meteor. Soc, pp. 48–51, 1998.

Van Rijsbergen, C. J.: Information retrieval. 2nd. newton, ma, 1979.

Waldvogel, A., Federer, B., and Grimm, P.: Criteria for the Detection of Hail Cells, Journal of Applied Meteorology and Climatology, 18, 1521–1525, https://doi.org/10.1175/1520-0450(1979)018<1521:CFTDOH>2.0.CO;2, 1979.

Wilks, D. S.: Statistical methods in the atmospheric sciences, vol. 100, Academic press, 2011.

Wu, Y., Kirillov, A., Massa, F., Lo, W.-Y., and Girshick, R.: Detectron2, https://github.com/facebookresearch/detectron2, 2019.

Wu, Y., Kirillov, A., Massa, F., Lo, W.-Y., and Girshick, R.: Detectron2, https://github.com/facebookresearch/detectron2/blob/main/detectron2/config/defaults.py, 2023.

Ziegler, C. L., Ray, P. S., and Knight, N. C.: Hail Growth in an Oklahoma Multicell Storm, Journal of Atmospheric Sciences, 40, 1768–1791, https://doi.org/10.1175/1520-0469(1983)040<1768:HGIAOM>2.0.CO;2, 1983.

Zou, Z., Shi, Z., Guo, Y., and Ye, J.: Object Detection in 20 Years: A Survey, https://doi.org/10.48550/ARXIV.1905.05055, 2019.
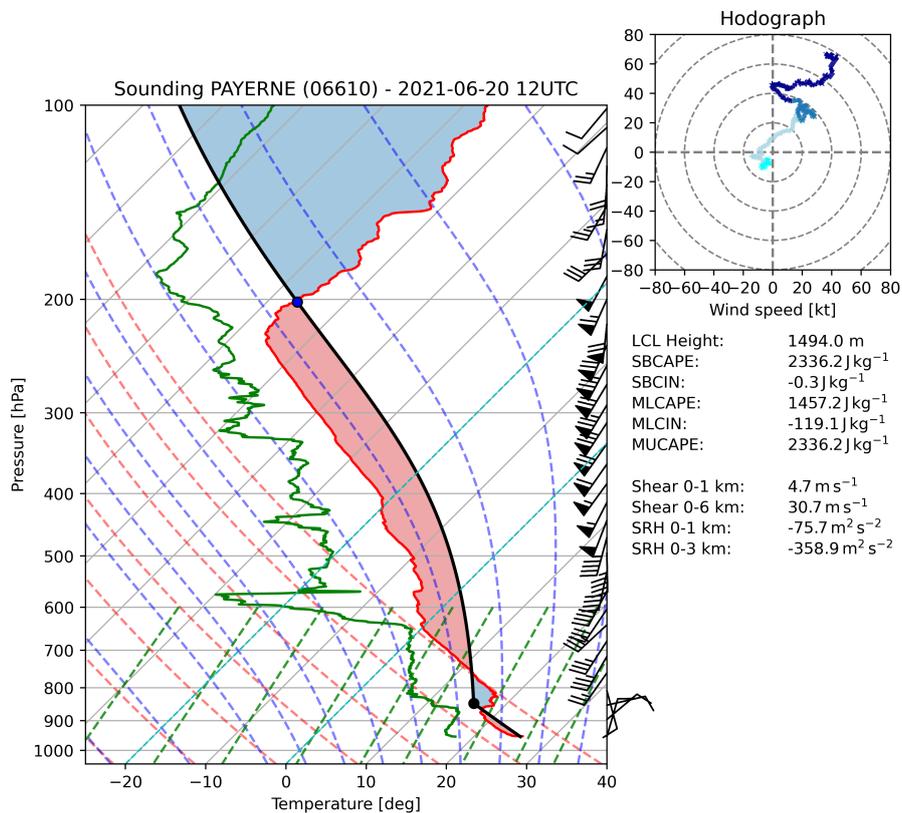
Figure 1. Skew-T plot with hodograph analysis from the atmospheric radio sounding at the Payerne station (ID: 06610, 87 km WSW from the soccer field) on 2021-06-20 12 UTC, produced with the MetPy software (May et al., 2023). The temperature and dew point profiles are drawn in red and green. The shaded areas in red and blue mark the CAPE (Convective Available Potential Energy) and CIN (Convective Inhibition). The hodograph display shows four layers: 0–1 km (cyan), 1–3 km (light blue), 3–5 km (blue), 5–10 km (dark blue).
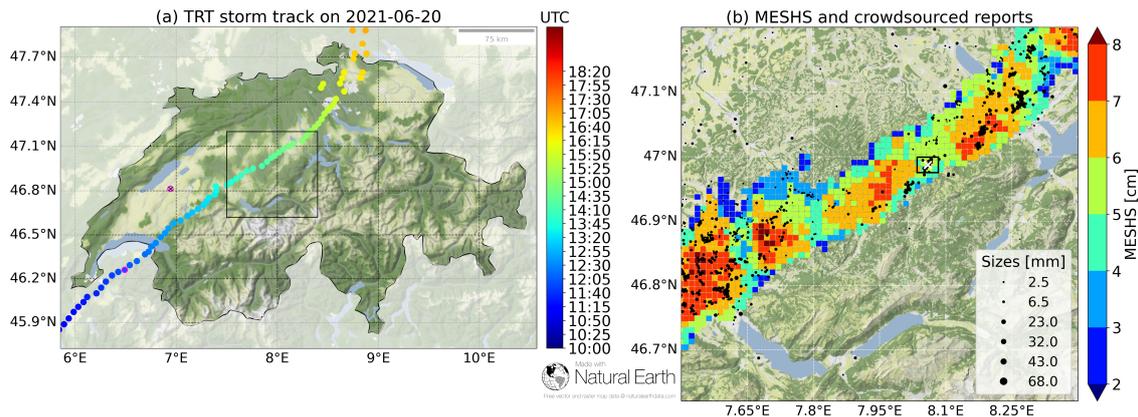
Figure 2. Storm track (a) of the 2021-06-20 supercell with colored time information (5 min resolution of the scatter points) and the location of the atmospheric radio sounding (magenta open circle with black cross inside) shown in Fig. 1. The storm location at the sounding time (12 UTC) is marked with the same edge color (magenta). The black rectangle in (a) marks the zoom area for plot (b), where information on radar derived MESHS (Maximum Expected Severe Hail Size) and crowdsourced hail size reports (black and different sized circles for 6 size categories with bin centers at 2.5, 6.5, 23, 32, 43 and 68 mm, are given. The location of the soccer field, where the drone-based hail survey took place, is marked with a white cross. The black rectangle around the white cross in (b) marks the zoom area for the detailed map view in Fig. 3. Map tiles by Stamen Design (stamen.com) and Stadia Maps (stadiamaps.com), under CC-BY-4.0. Map data copyrighted by OpenStreetMap contributors under CC-BY-SA and available from https://www.openstreetmap.org.
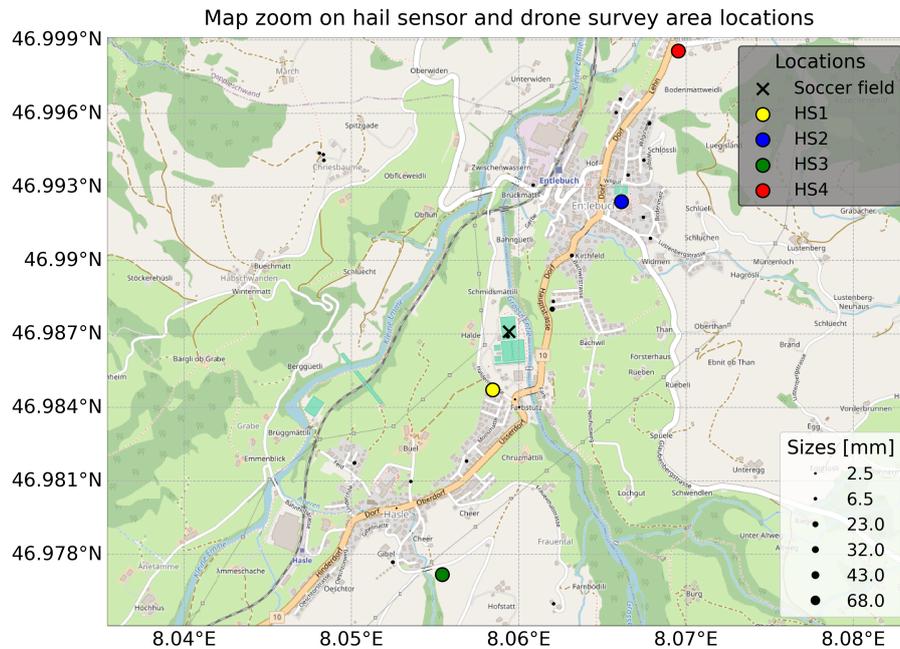
Figure 3. The zoom area and detailed view for the marked black rectangle around the white cross in Fig. 2(b). It shows the locations of the soccer field (roughly centered to the map view, black cross), the 4 nearest automatic hail sensors (HS1, HS2, HS3 and HS4) and the crowdsourced hail size data (black and different sized circles). Map tiles by Stamen Design (stamen.com) and Stadia Maps (stadiamaps.com), under CC-BY-4.0. Map data copyrighted by OpenStreetMap contributors under CC-BY-SA and available from https://www.openstreetmap.org.
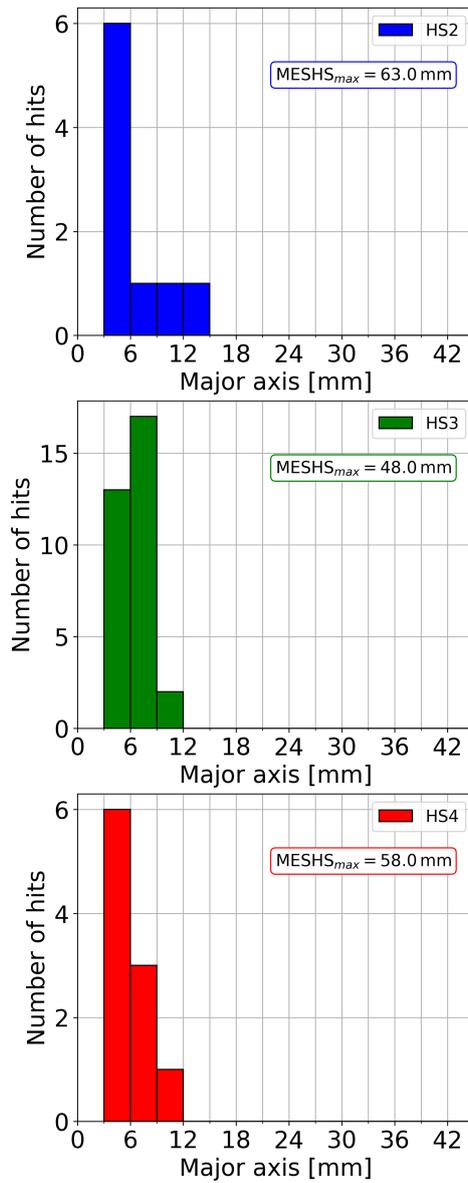
Figure 4. Histograms of the recorded hail size distributions from the automatic hail sensors together with the daily maximum MESHS value at the sensor locations (see Fig. 3). The recorded hail duration for the sensors are about 3 min (HS2), 16 min (HS3) and 13 min (HS4). The color scheme follows the one from Fig. 3. The HS1 sensor did not record any hailstones, and is thus omitted here.
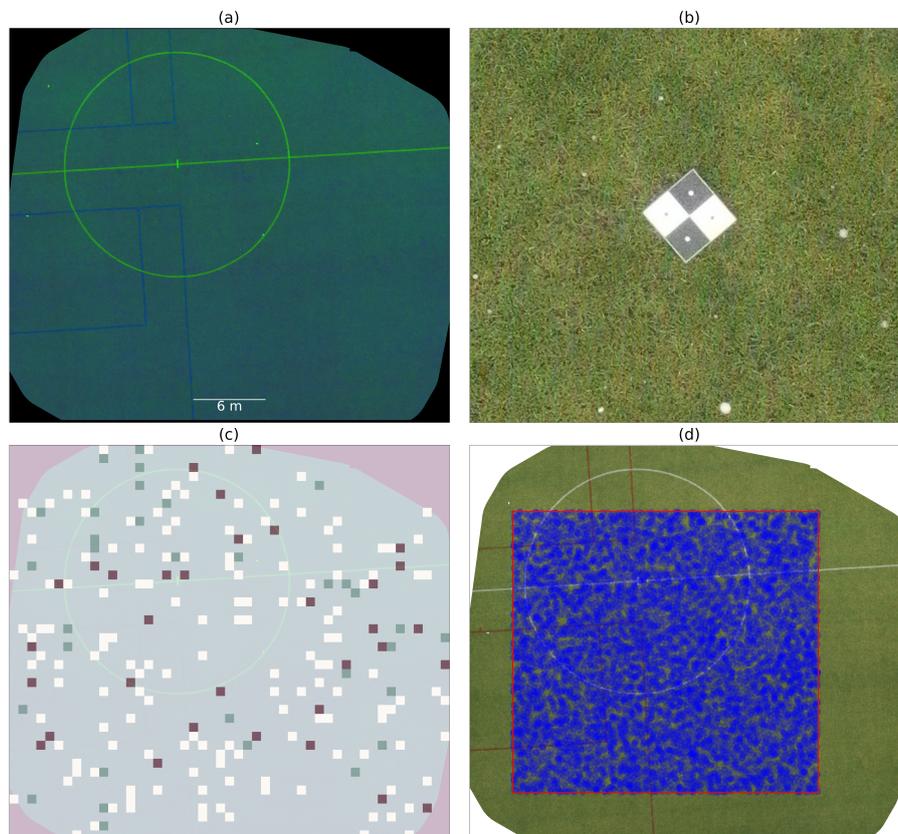
Figure 5. In (a), the final orthophoto of the 2021-06-20 hail event is shown in HSL (Hue, Saturation, Lightness) color space. It is produced from 116 individual aerial drone images with the OpenDroneMap (ODM) software package. The radius of the soccer middle circle is $9.15\,\mathrm{m}$. In (b) an image zoom from the orthophoto with actual scale of $1\,\mathrm{m}$ (width) and $0.9\,\mathrm{m}$ (height) illustrates the hail appearance on the soccer field in conjunction with one of the reference objects (black and white circles: $10\,\mathrm{mm}$ diameters; black and white squares: $75\,\mathrm{mm}$ side lengths) to verify the ground sampling distance (GSD). In (c), the random selected distribution of training (light grey), validation (green) and test (dark red) image tiles ($75\,\mathrm{cm}$ edge length) are displayed within the orthophoto. Plot (d) belongs to Sect. 3.2 and displays the same orthophoto in RGB (Red, Green and Blue) color space over-plotted by a $600\,\mathrm{m}^2$ area (red rectangle), where 10000 circles of $0.2\,\mathrm{m}^2$ (virtual hail sensors, blue shaded) are randomly placed for statistical assessments.
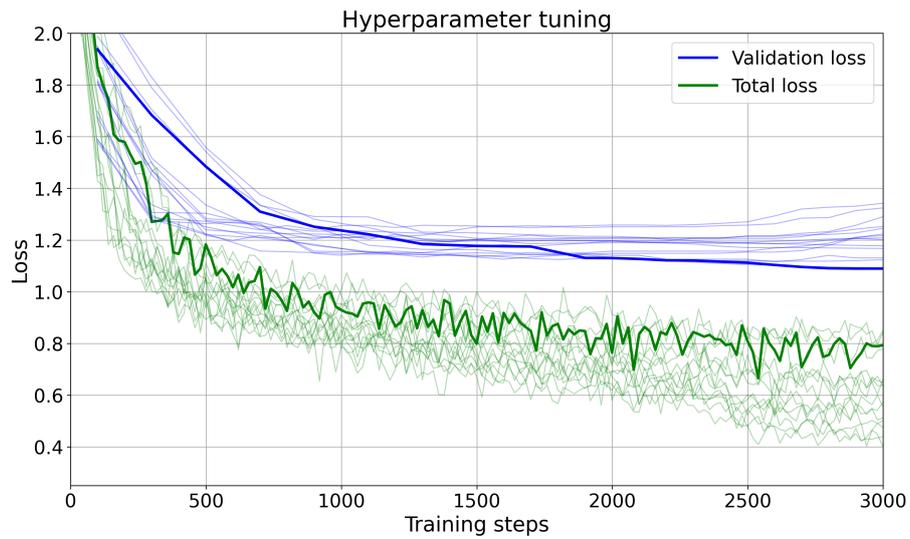
Figure 6. Line plots of the evolution of validation loss and total loss along the training iteration steps for the 16 deep-learning model runs with different combinations of hyper-parameters shown in Table 2. The thick lines depict the training *run-3*, used for prediction of hail pixels.
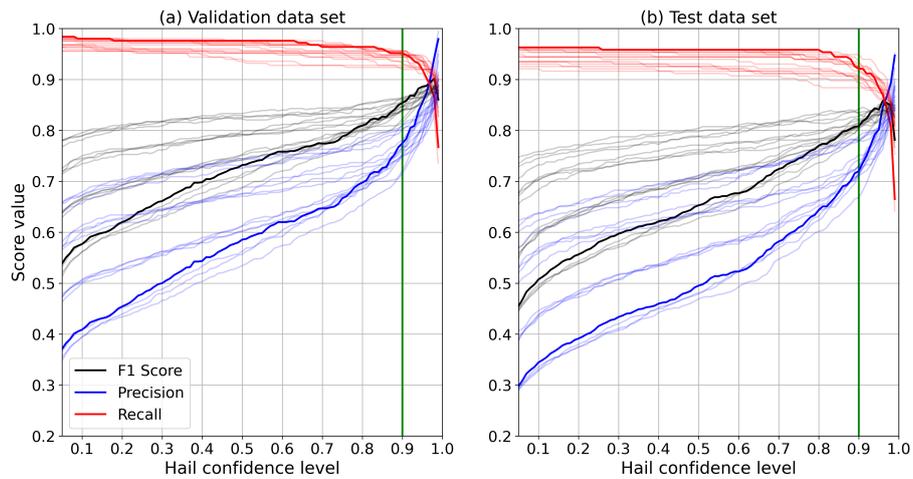
Figure 7. Spaghetti plots of precision (blue), recall (red) and $F1$ scores (black) against the hail confidence level for all 16 deep-learning model runs applied to the validation data (a) and test data (b). The thick lines depict the training *run-3*, used for prediction of hail pixels. The green vertical line marks the $90\,\%$ hail confidence value, that has been chosen as the lower limit for the object classification.
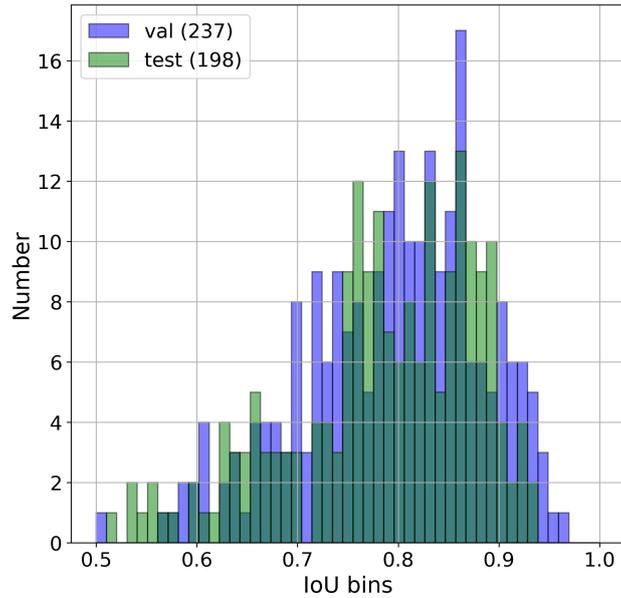
Figure 8. Histograms of IoU (Intersection over Union) ratios between model *run-3* prediction masks (hail confidence $C_i \geq 0.9$) and the validation data set (blue), respectively the test data set (green). The histogram area of the overlap between green and blue bars appears in dark green color. Only true positive (TP) matches, defined as IoU > 0.5, are shown. In the validation (test) data set 237 (198) hailstones are classified as TP.
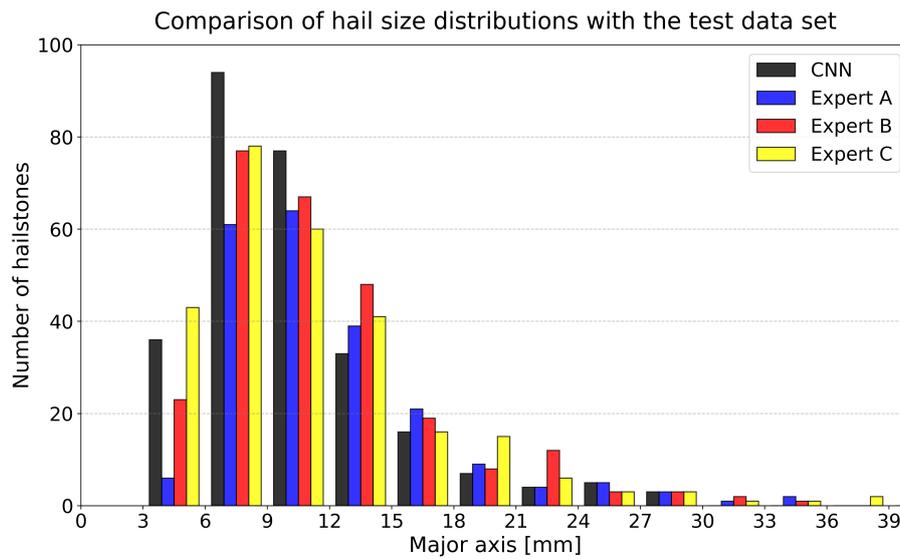
Figure 9. Comparison of four hail size distributions from the test data set derived from manual annotations by three experts (A: blue, B: red, C: yellow) and the prediction of the Mask R-CNN model (black). The total number of identified hailstones by the experts are 215 (A), 263 (B) and 269 (C). The CNN (Convolutional Neural Network) predicted 275 hail segmentation masks.
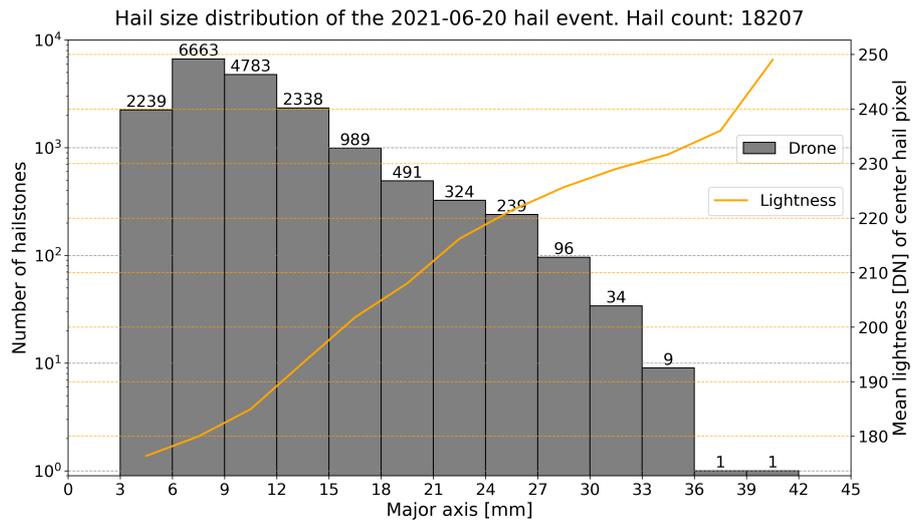
Figure 10. Logarithmic view of the time integrated hail size distribution of the 2021-06-20 event captured by the drone between 14:37:28 and 14:41:19 UTC. The total number of detected hailstones per each bin is shown with the number above each bar. All together 18207 hailstones were identified. The orange line represents the mean lightness value as digital number (DN) of all derived center hail pixels in the HSL (Hue, Saturation, Lightness) color space for each hail size bin.
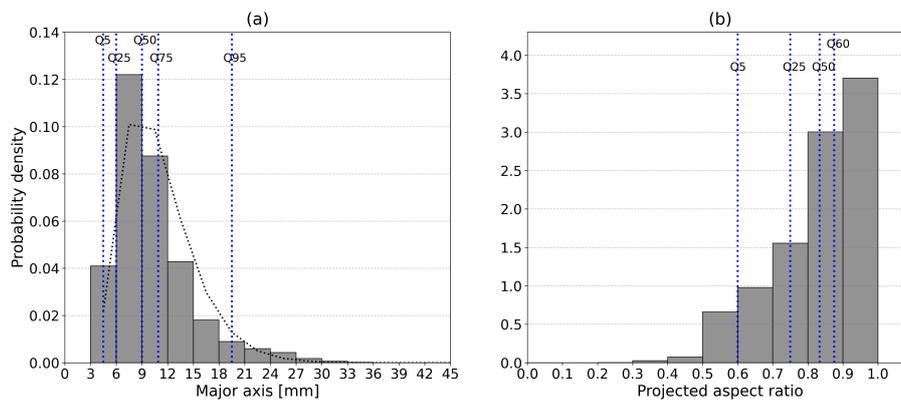
Figure 11. Probability density distributions of the hail major axis (a) and the projected aspect ratio (b) between minor and major axis length in the image plane. The vertical blue dashed lines indicate the position of the particular quantiles with respect to the major axis (Q5, Q25, Q50, Q75, Q95) and projected aspect ratio (Q5, Q25, Q50, Q60). The HSD in plot (a) is additionally fitted against a gamma distribution (black dotted line).
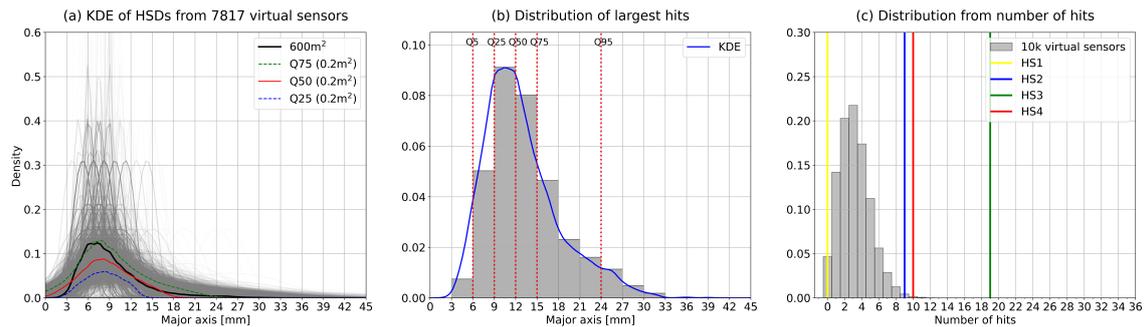
Figure 12. Kernel density estimation (KDE) of HSDs (Hail Size Distributions) from simulated hail sensors at random locations (a) on an area of $600\,\mathrm{m}^2$ (red rectangle in Fig. 5(d)). From the 10000 virtual HSDs 7817 can be represented by a KDE (gray curves), whereas the others do not have enough impacts. The quantiles of the sorted HSDs are shown as dashed blue (Q25), dashed green (Q75) and solid red (Q50) curves. For comparison, the KDE as derived from the whole $600\,\mathrm{m}^2$ area is overplotted in black. In the center (b), the KDE distribution for the aggregation of the largest hailstone impact on each virtual sensor is shown. Quantile markers (Q5, Q25, Q50, Q75, Q95) are drawn on top of plot (b) in dashed red vertical lines. On the right side (c), the probability density for the total impacts on each virtual sensor is shown as gray histogram, together with the registered number of impacts of the four closest automatic hail sensors HS1 (cyan line), HS2 (blue line), HS3 (green line) and HS4 (red line).
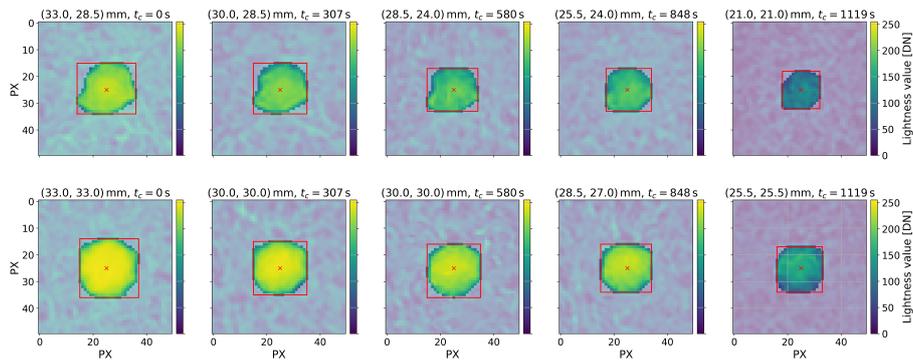
Figure 13. Two examples of hailstone size and mask shape development during the captured melting process on the ground. From left to right the sequential lightness images of two hailstones (row 1 and 2) extracted from the five orthophotos (soccer middle circle) are shown. In the images the Mask R-CNN segmentation masks are emphasized together with with the major and minor axis lengths indicated by the minimal bounding boxes. The actual sizes (width, height) are given in the titles as well as the the time t_c since first capture. During the $1119\,\mathrm{s}$ these hailstones shrink about $12\,\mathrm{mm}$ (upper row) and $7.5\,\mathrm{mm}$ (lower row) in their major axis length.
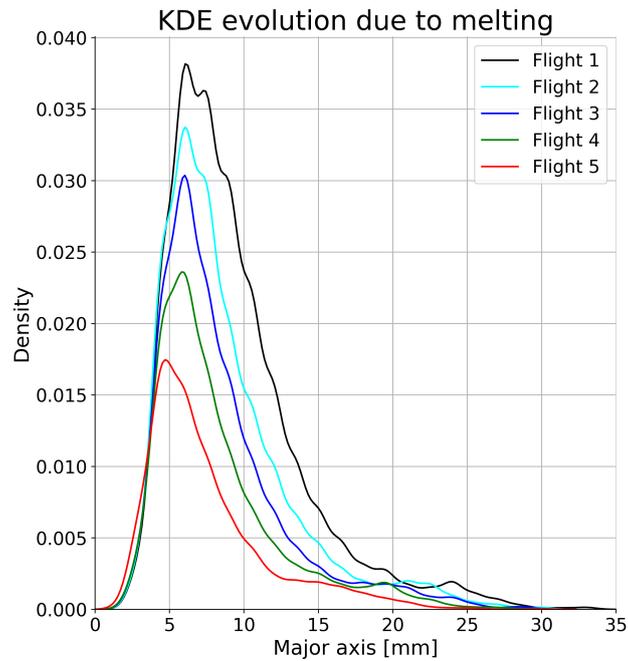
Figure 14. Kernel density estimation (KDE) of the degrading hail size distributions due to melting processes on the ground. The initial hail sample size is 3925. The orthophoto area for the melting analysis is restricted to the soccer middle circle to ensure a correct comparison between the different generated orthophotos (Flight 1–5). In total, five drone-based hail photogrammetry surveys were carried out to capture the temporal data analysis. All the relevant time frames are listed in Table 3.
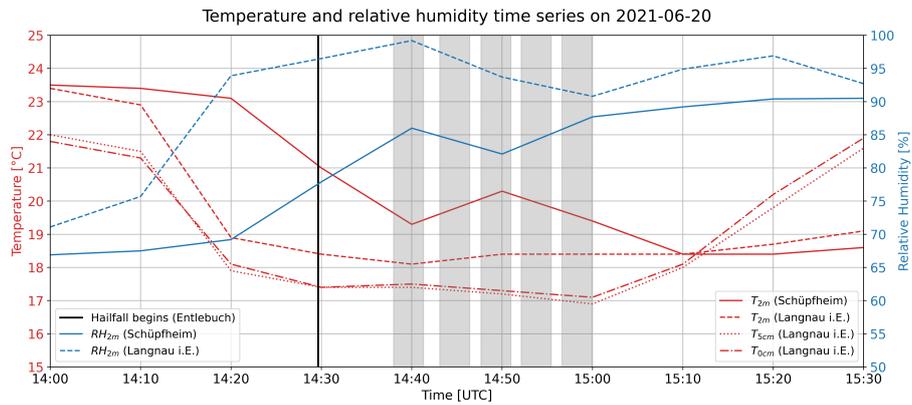
Figure 15. Measurement time series of temperature (red lines) at $2\,\mathrm{m}$ (T_{2m}), $5\,\mathrm{cm}$ (T_{5cm}), ground-level (T_{0cm}) and relative humidity (blue lines) at $2\,\mathrm{m}$ (RH_{2m}) from the SwissMetNet (SMN) weather station in Langnau i.E. ($744\,\mathrm{m\,a.s.l.}$) and measurement time series of T_{2m} and RH_{2m} from the SMN weather station in Schüpfheim ($744\,\mathrm{m\,a.s.l.}$) on 20 June 2021 between 14:00 and 15:30 UTC. The beginning of the hailfall in Entlebuch is marked as black vertical line and the duration of the drone flights to capture the soccer middle circle are marked as grey shaded bars.